Journal of Physics: Conference Series **3224** (2026) 042040 doi:10.1088/1742-6596/3224/4/042040

Effects of aero-elastic blades on a floating offshore turbine subjected to an imposed surge motion

E Mascrier[1], F Zilic de Arcos[1,2] and G Pinon[1]

[1] Laboratoire Ondes et Milieux Complexes (LOMC) - Normandie Univ, UNIHAVRE, CNRS, Le Havre, France

[2] Department of Engineering Science, University of Oxford, Oxford, UK

E-mail: enzo.mascrier@etu.univ-lehavre.fr

Abstract. This article presents a numerical study of the NREL 5MW rotor equipped with elastic blades subjected to surge motion. An in-house fluid-structure interaction model based on coupled actuator-line method with Timoshenko beam model is presented. Both methods are verified using reference cases from the literature for fixed and surging rotors showing good agreement. Aerodynamic forces on the surging rotor are compared between elastic and rigid blades. In the tip region, the flexible rotor experiences lower forces due to large deflections which reduce local angle of attack. The wake development is also affected by blade structural deformation, although its influence remains limited under the investigated conditions.

1. Introduction

Over the last 20 years, the rated power of both onshore and offshore turbines has increased significantly. The average rotor diameter of offshore turbines rose from 80 meters in 2002 to 160 meters in 2020 in Europe [1]. These values are expected to increase further in the coming years. For floating offshore wind turbine, larger diameters lead to increased dynamic effects on both rotor blades and floating platforms.

Turbine blades are complex structures typically composed of carbon and glass reinforced plastics, with foam as core material, and one or several internal shear webs [2]. The structural design allows the blade to bend when it is subjected to external loads. Tip displacements are becoming larger with the diameter increase. This raises questions about fatigue and rotor performance. Zilic de Arcos et al. [3] showed that blades with an initial static deformation have an impact on rotor power and thrust for different levels of tip deflections. However, to fully understand the impact of blade deflections on rotor aerodynamics, under steady and unsteady flow conditions, dynamic effects also need to be taken into account.

Fluid-structure interaction (FSI) models coupling a dynamic structural solver with an aerodynamic model can be found in the literature. Many of them are based on the blade element momentum theory (BEMT) like OpenFAST [4]. Because the BEMT is a simplified aerodynamic model that relies on two-dimensional lift and drag coefficients and assumes annular section independence, it cannot capture all the blade bending induced effects on the flow, rotor loads and performance. Computational fluid dynamics (CFD) methods are necessary to model these effects. Dose et al. [5], e.g, used blade-resolved (BR) simulations with the Geometrically Exact Beam Theory (GEMT) to describe FSI phenomena on a wind turbine blade. The computational

time required for this method can be significant because of the large number of cells required to resolve the blade geometry and the use of morphing meshes to account for blade deflections in the aerodynamic model. Results show a decrease in the generated power and an increase in the angle of attack near the blade tip. Similar observations for the power have been reported in other studies [6, 7].

Rotor displacement induced by floating platform motions also affects turbine performance. Surge and pitch motions are the main drivers of unsteady loads in floating offshore wind [8]. The International Energy Agency (IEA) coordinates the Offshore Code Comparison project. Its objective is to investigate the impact of floating platform motion on turbine aerodynamic and structural dynamics [9].

The present study specifically investigates the surge motion. Rotor plane normal oscillations introduce a time-dependent variation of parameters like power and thrust [10]. Integrated parameters show a strong dependency on the imposed surge frequency and amplitude [11]. The surge motion induces an additional velocity component experienced by the rotor, which is directly related to the surge frequency and amplitude [12]. To the best of the author's knowledge, the impact of surge motion on elastic blades remains insufficiently described in the existing literature, particularly regarding local aerodynamic quantities such as angle of attack variations and wake development, e.g Liu et al. [6] mainly presented integrated parameters such as root bending moment or power.

In this study, the NREL 5MW rotor [13] is used to study FSI phenomena of a wind turbine undergoing surge motions. This rotor was chosen because it matches the power output and size of rotors employed in offshore floating wind turbines [14]. An in-house Actuator-Line Model (ALM) [15] is chosen to simulate the turbine aerodynamic, and is coupled with an in-house dynamic structural model based on the Timoshenko beam theory [16] to capture blade structural dynamics.

The aerodynamic and structural models are presented in the Section 2. In Section 3.1, the structural solver is used to analyse the rotor at rated condition [5] with and without a prescribed harmonic surge motion [6]. In Section 3.2, the effects of the surge motion on elastic blades are discussed at a fixed amplitude and frequency. Conclusions are presented in Section 4.

2. Numerical method

2.1. Inflow and motion conditions

In this study, the NREL 5MW rotor is simulated at its rated conditions: a uniform non-turbulent inflow of $U_\infty = 11.4\,\mathrm{m.s^{-1}}$ and a tip speed ratio of $\lambda = 7$. The rotor is initially studied without surge motion in the Section 3.1.1. Thereafter, the rotor is subjected to a sinusoidal surge displacement with a fixed amplitude ($A_m = 10\,\mathrm{m}$) and period ($T_{surge} = 12\,\mathrm{s}$). Similar frequencies are used in the literature to describe surge motions [17, 18]. The amplitude is increased to highlight aeroelastic effects on performance and wake compared to other studies [18].

2.2. CFD model

We conducted simulations using a Finite Volume Method (FVM) CFD model with Large Eddy Simulation (LES) turbulence modelling the Smagorinsky subgrid-scale approach [19]. The Smagorinsky coefficient is set to 0.17 in accordance with the literature [20]. The PIMPLE algorithm is used to solve the incompressible Navier-Stokes equations through pressure-velocity coupling. PIMPLE combines the SIMPLE and PISO algorithms to improve numerical stability and solution convergence. The computational domain has a rectangular cross section, length of 22 diameters along the flow direction, with 9.5 diameters in the directions perpendicular to

the flow, and a 3.46 % area blockage. The fluid domain is discretised with a structured grid containing cubic hexahedral cells. A higher-resolution mesh is employed around the turbine, whereas the background domain is discretized with a mesh size of $\Delta x_{background} = 18.18$ m. The refined turbine region features a mesh size of $\Delta x_{turbine} = 1.14$ m, corresponding to 110 cells per diameter. Mesh refinement is applied around the turbine in a box that extends to the downstream boundary of the domain and has a width of 1.35D in the transverse directions, with smooth transitions ensured through a succession of refinement boxes.

2.3. Actuator-Line Method

The Actuator-Line Method was introduced for wind turbine blades in 2002 by Sørensen and Shen [15]. The model was initially developed to model wind turbine wakes and performance with an increased fidelity compared to actuator disk methods. ALM prevents reproducing the blade geometry and solving the blade boundary layer, thus reducing the computational costs compared to BR simulations. The method has been extensively validated against experimental data and blade-resolved simulations, demonstrating its ability to accurately predict aerodynamic loads and wake characteristics for a wide range of operating conditions [21, 22].

Turbine blades are represented by rotating lines discretized into actuator points. The flow velocity is sampled around each actuator point using the Line Average Sampling (LAS) presented in [23] and adapted to the ALM by Zormpa et al. [24]. The LAS sampling radius is defined to $r_s = 1.1 \cdot 3\epsilon$ with ϵ the standard deviation of the Gaussian force smearing set to $\epsilon = 2\Delta x_{turbine}$. On each collocation point, lift and drag forces are calculated using tabulated lift and drag coefficients from [13] (C_L and C_D, respectively) based on local angle of attack (α). Aerodynamic forces acting on each blade section are reconstructed from the lift and drag components. The resulting body force is distributed onto the flow using a Gaussian distribution. Tip loss effects are corrected using the Shen model [25]. Fig 1 shows the rotor represented by actuator lines with forces applied on each blade section.

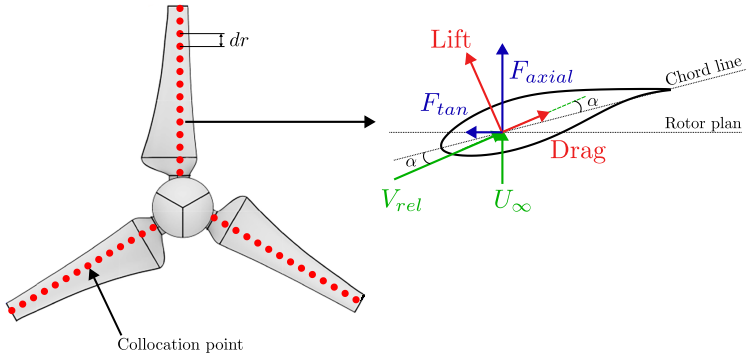

Figure 1. Rotor modelled with the ALM. Red dots represent collocation points where lift and drag coefficients are calculated. The blade section illustrates the aerodynamic forces acting at the position

Body forces computed by the ALM are introduced to the discretised Navier-Stokes equations as a source term $\mathbf{f_s}$.

$$\nabla \cdot \mathbf{u} = 0 \tag{1}$$

$$\frac{\partial \mathbf{u}}{\partial x} + (\mathbf{u} \cdot \nabla)\mathbf{u} = -\nabla P + \nu \nabla^2 \mathbf{u} + \nabla \cdot \tau_{sgs} + \mathbf{f_s} \tag{2}$$

$\mathbf{u}$ represents the flow velocity in the cell, P the pressure and τ_{sgs} the sub-grid scale stress. The system is discretised and resolved using the method presented in Section 2.2.

2.4. Structural model

The ALM is coupled with an in-house structural solver based on the dynamic Timoshenko beam theory [16] to compute blade deformations. Unlike the Euler-Bernoulli beam theory, the Timoshenko formulation accounts for the shear deformation resulting in blade section rotation. The governing equations are :

$$\begin{cases} \rho_s A \frac{\partial^2 u_s}{\partial^2 t} = \frac{\partial}{\partial x}[\kappa AG(\frac{\partial u_s}{\partial x} - \phi)] \\ \\ \rho_s I \frac{\partial^2 \phi}{\partial^2 t} = \frac{\partial}{\partial x}(EI\frac{\partial \phi}{\partial x}) - \kappa AG(\frac{\partial u_s}{\partial x} - \phi) \end{cases} \tag{3}$$

with ρ_s the material density, A the cross-section area, κ the Timoshenko shear coefficient, G and E respectively the shear and elastic modulus and I the second moment of area. u_s represents the displacement of the mid-surface and ϕ is the cross-section angle to the initial beam angle. The parameters are shown in Fig 2.

The system is discretized using the finite element method. The Timoshenko beam element is given by :

$$M^e \left\{\ddot{q_e}\right\} + C^e \left\{\dot{q_e}\right\} + K^e \left\{q_e\right\} = F^e \tag{4}$$

with M^e, C^e and K^e the elementary mass, damping and stiffness matrices respectively, F^e is the external force vector, composed of aerodynamic loads acting on the structure. $\left\{q_e\right\}$ is a vector containing the out-of-plane (u_f and ϕ_f) and in-plane (u_e and ϕ_e) displacement and the torsional angle ($\phi_{torsion}$), presented in Fig 2. The damping matrix is modelled with the Rayleigh method :

$$C^e = \alpha_R M^e + \beta_R K^e \tag{5}$$

This approach offers a convenient implementation since it is based on a linear combination of the stiffness and mass matrices. α_R and β_R are determined from blade natural frequencies and a specified structural damping ratio of $\zeta = 0.478\%$. In this study, the chosen parameters are $\alpha_R = 5.2324$ and $\beta_R = 0.1798$.

The final system is assembled by combining all beam elements and solved by using the second-order Newmark algorithm presented in [26]. This approach is unconditionally stable.

The Timoshenko solver and the ALM are coupled with a two-way strong coupling, allowing for mutual exchange of aerodynamic loads and structural deformations. The coupling algorithm can be divided in six steps : the blade position is transferred from the structural solver to the actuator-line model during step (1). Forces along the blades are computed during step (2) and transferred to the structural solver in step (3) to determine the deformed blade shape during step (4). The updated position is exchanged again with the actuator-line in step (5). Finally, the forces are computed and applied to the flow at the correct blade coordinates in step (6). The coupling scheme is carried out once per timestep. A schematic of the inter-model data transfer and computation order is shown in Fig 3.

3. Results

3.1. FSI simulations verification

3.1.1. Under steady flow conditions A fixed rotor configuration, neglecting surge motion, is used to verify the proposed numerical method. Aerodynamic forces acting on the blades are compared with the BR results of Dose et al. [5] in Fig 4. Similar results are found between our ALM results and the reference study. Discrepancies can be attributed to different modelling

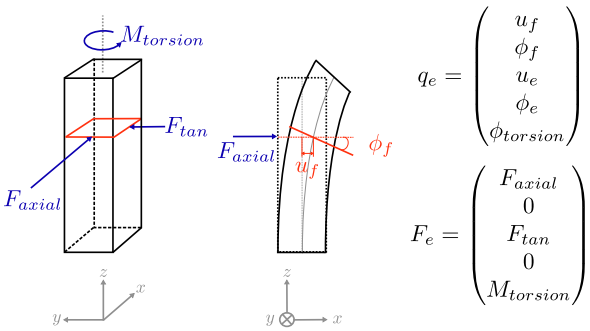

Figure 2. 3D Timoshenko beam representation showing the system variables

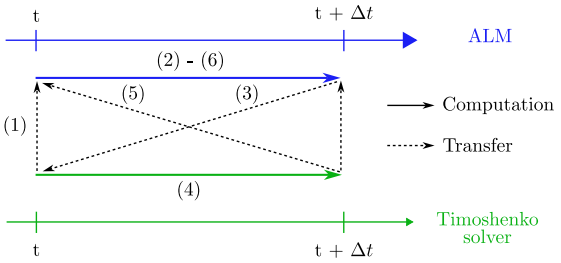

Figure 3. Two-way coupling between the ALM and the Timoshenko beam structural solver, including the exchange of aerodynamic loads and blade deformations

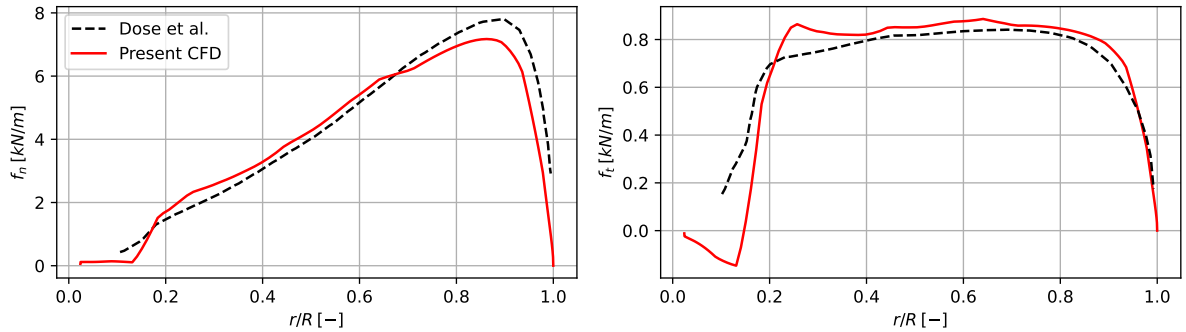

Figure 4. Normal (left) and tangential (right) forces acting on the blade without deformations compared to Dose et al. [5]

approaches. Unlike BR simulations, our ALM relies on tabulated polar coefficients and uses a tip loss correction method which leads to the modest load differences observed.

The ALM coupled with the structural solver presented in Section 2.4 is used to investigate blade flexibility. Deflections in the out-of-plane (flapwise), the in-plane (edgewise) and the torsional deformation are determined for the rated flow condition. Results for bending and torsion at the tip are given in Table 1. Good agreement is found with the results of Dose et al. for the rotor case without surge motion (fixed rotor). As with the rigid blades, modest discrepancies exist between the forces predicted by the ALM and the blade-resolved simulations. Since these forces serve as input to the structural solver, the lower normal force results in a reduced out-of-plane blade displacement. However, the observed differences remain acceptable to the authors' point of view.

Table 1. Comparison between ALM-Timoshenko and BR-GEMT (Dose et al. [5]) for out-of-plane, in-plane and torsional deformation for the fixed rotor with elastic blades

Deformation	ALM-Timoshenko	Dose et al.	Difference [%]
Out-of-plane [m]	5.46	5.55	1.62
In-plane [m]	-0.63	-0.62	1.61
Torsion [°]	0.28	0.29	3.45

3.1.2. Under unsteady condition Following the verification of the static case, the rotor is tested under unsteady conditions. The rotor is prescribed an oscillatory surge motion following Eq (6):

$$x(t) = A_m \, sin(\omega_s t) \tag{6}$$

CFD simulations from Liu et al. [6] are used to benchmark our results. In this analysis, the rotor undergoes oscillatory surge with an amplitude of $A_m = 2$ m and a period of $T = 12$ s. The resulting reduced frequency $k = \omega_s R/U_\infty$ is 2.89 corresponding to a strongly unsteady case. Flapwise and edgewise deflections over the last surge motion phase ϕ_s are presented in Fig 5. A good agreement is observed between our results and those of Liu et al. with 1.39 % and 4.46 % difference in peak flapwise and edgewise deflections. The modest differences may be associated with a different handling of damping, with the damping matrix modelled using the Rayleigh method, and due to the 2.5° precone angle imposed in the reference study. Considering the minor observed differences, the model is considered adequate for studying surge motions.

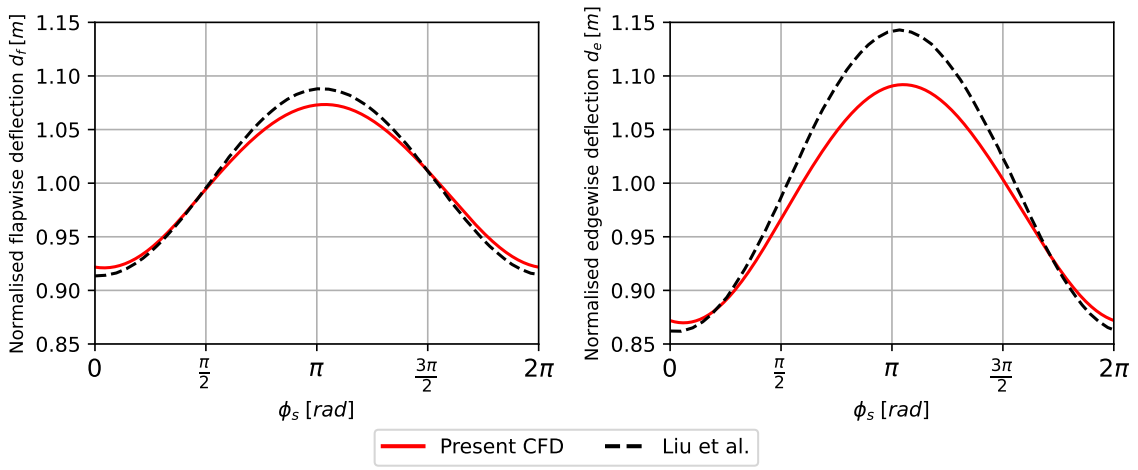

Figure 5. Normalised flapwise and edgewise deflections over the last surge period compared with Liu et al. [6]

3.2. Turbine with elastic blades subjected to surge motion
Aeroelastic effects are examined with the rotor undergoing surge oscillations under parameters presented in Section 2.1. Four configurations are investigated: a fixed rotor with rigid blades (Fix-Rig), a fixed rotor with flexible blades (Fix-Fle), a surging rotor with rigid blades (Sur-Rig), and a surging rotor with flexible blades (Sur-Fle). These abbreviations are used hereafter. In Section 3.2.1, effects on the rotor performance are discussed while the wake development is investigated in Section 3.2.2.
3.2.1. Rotor performance Fig 6 shows the power (C_P) and thrust (C_T) coefficients during a surge period. Results are compared with a reference fixed rotor case with rigid and flexible blades.

The time-averaged power and thrust coefficient over the last ten surge periods are presented in the Table 2. Minor differences in the time-averaged power coefficient are observed between the cases. For the Fix-Rig case, a power coefficient C_P of 0.503 is obtained. C_P decreases by 3.78 % for the Fix-Fle configuration, which is consistent with previously reported results [6]. When the rotor is subjected to surge, the Sur-Rig achieves $\overline{C_P} = 0.523$, whereas the Sur-Fle shows a lower value of $\overline{C_P} = 0.499$. However, the maximum C_P for the Sur-Rig case is higher compared to Sur-Fle, corresponding to a 4.59 % difference. Regarding the thrust coefficient,

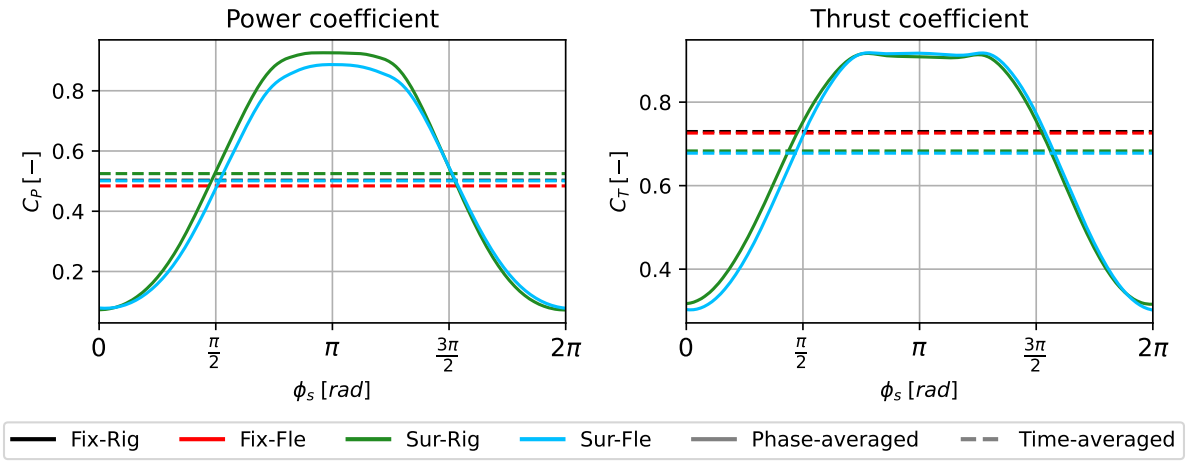

Figure 6. Phase-averaged power and thrust coefficient variable over the surge period. The continuous lines represent the phase-averaged variation over the last ten surge periods, while the dashed lines represent the time-averaged values over the same period, summarised in the Table 2

Table 2. Time-averaged coefficients for the four cases presented in Fig 6

Rotor configuration	Time-averaged power coefficient	Time-averaged thrust coefficient
Fix-Rig	0.503	0.730
Fix-Fle	0.484	0.726
Sur-Rig	0.523	0.682
Sur-Fle	0.499	0.676

variations are less evident but slightly more pronounced in the flexible configuration. The mean thrust coefficient $\overline{C_T}$ is decreased for the surging turbine. $\overline{C_T}$ between the fixed and the surging rotor is reduced by 3.50 % for rigid blades and 6.89 % for flexible blades.

Forces distribution is presented in Fig 7. Surge motion leads to a reduction in the mean normal force. The diminution is even more important for the flexible blade, especially at $r/R > 0.7$. This region corresponds to the blade section with the largest deformation. Since both the surge velocity and the blade motion due to bending have components along the flow direction, the forces near the tip experience amplified fluctuations. In the out-of-plane direction, the deformation varies from 4.75 % to 10.61 % of the blade radius at the tip. Deformation also induces an out-of-plane rotation of the blade elements, modifying force orientation and thus, time-averages and fluctuations. The mean tangential force varies significantly compared to the fixed case. For both Sur-Rig and Sur-Fle cases, the mean force decreases in the radial range $0.2 < r/R < 0.3$ while an increase is observed for Sur-Rig rotor on the upper half of the blade ($r/R > 0.45$). In contrast to the normal force behaviour, larger fluctuations are observed for their tangential components for the rigid blade. The in-plane deflection is limited, varying from 0.48 % to 1.43 % of the blade radius. This reduction is sufficient to decrease the mean tangential force near the blade tip, while preserving a variation range comparable to the rigid case.

The rotor experiences an additional velocity component induced by the surge motion, which consequently alters relative inflow speed and the angle of attack, as seen in Fig 8. Within the region where $r/R < 0.9$, the Sur-Rig turbine exhibits a higher mean angle of attack compared to the Fix-Rig case. Changes in the angle of attack explain the tangential force variation in Fig. 7.

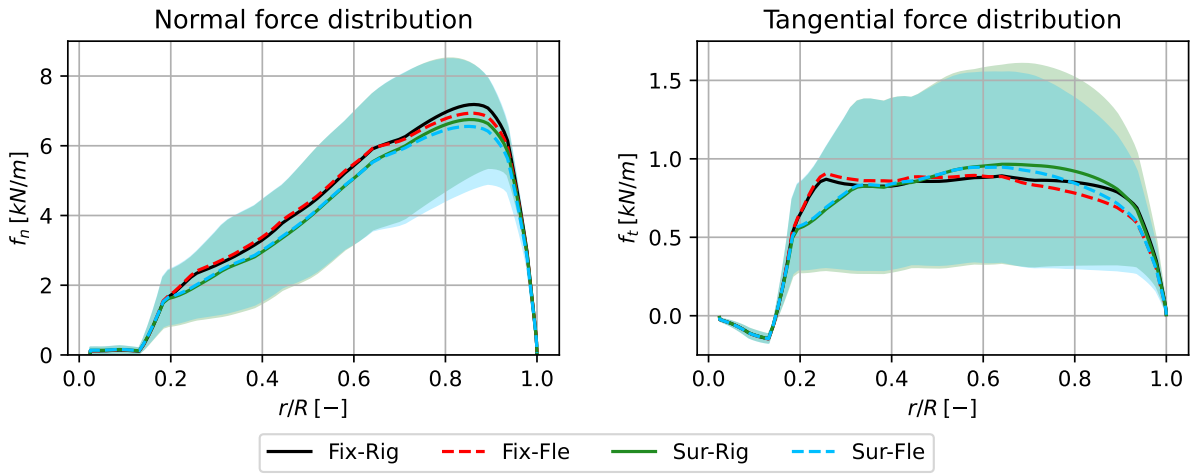

Figure 7. Normal and tangential force distribution along the span. Colour lines represent the time-averaged force during the last ten surge periods and the shaded parts represent the standard deviation around the time-averaged value (only for the surging rotor).

A higher angle of attack for the rigid blade leads to higher lift and drag coefficient, as prescribed by the aerodynamic polar used as input, and consequently a modification of the tangential forces. Nonetheless, the normal force decreases for both surging configurations compared to the fixed rotor, indicating that the surge motion is the dominant factor in the normal direction.

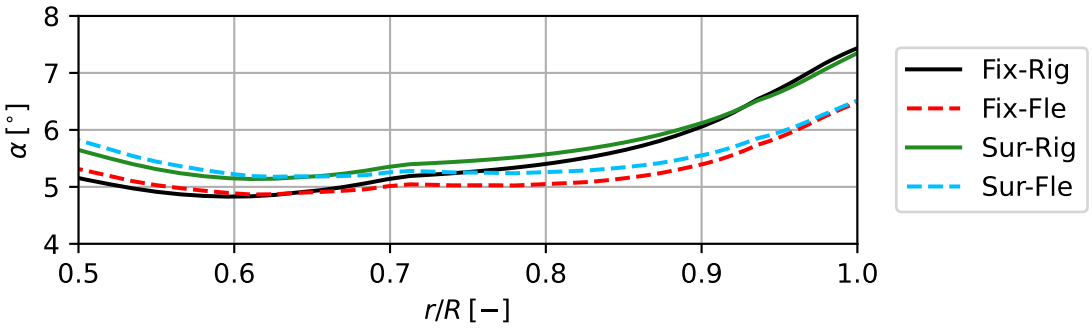

Figure 8. Spanwise distribution of time-averaged angle of attack

Variations of the angle of attack along the blade over a surge period are shown in Fig 9. The NREL 5MW blade is composed of multiple aerodynamic profiles, with stall angles around 10°. The surge motion drives the blade to operate beyond the stall angle and leads to increased force variability. In the present ALM, only steady polar coefficients are employed. Consequently, the simulations may not fully capture the relevant unsteady aerodynamic effects, since the blade operates beyond the static stall angle.

The flexible blades operate for less time above the stall angle compared to the rigid case, especially around the blade tip. As the blade oscillates around the stall angle, the lift coefficient will also oscillate around its maximum, whereas this is not the case for the drag coefficient. Consequently, surge motion leads to a higher mean tangential force and a lower mean normal force.

Overall, the surge motion has a limited impact on time-averaged power and thrust coeffi-

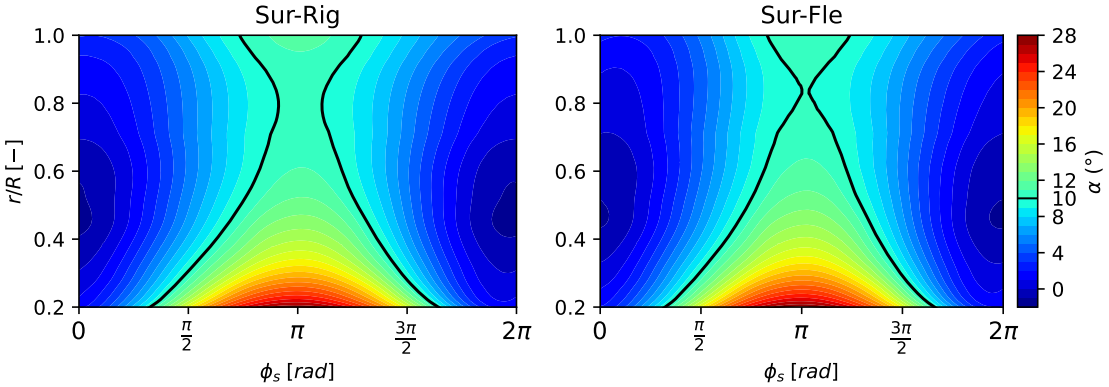

Figure 9. Time-averaged angle of attack distribution along the blade over the last five surge oscillations. Black lines represent points where $\alpha = 10°$, corresponding to a critical angle of attack for the stall

cients. Blade flexibility leads to a modest reduction in the mean power and thrust. At the blade scale, surge motion induces a more substantial modification to force distributions. A reduction in the mean normal force is observed, particularly in the outer blade region where structural deformation is more pronounced. In contrast, the mean tangential force remains close to the fixed-rotor case, with increased inboard loads for the surging blades and larger associated fluctuations. These effects are primarily driven by changes in the relative inflow velocity and angle of attack induced by surge motion.

3.2.2. Wake development Mean velocity profiles are shown in Fig 10. For the fixed rotor configuration, blade elasticity appears to induce no significant modification to the wake at the considered positions. However, the velocity deficit is less pronounced for the surging rotor, indicating a faster mixing between the surrounding flow and the wake. This is consistent with the C_T values reported in Table 2. Similar wake developments are observed in the near wake region between Sur-Rig and Sur-Fle configurations. The velocity deficit is less pronounced for Sur-Fle at $x/D = 1$. Forces in the streamwise direction are reduced when the blade undergoes bending, leading to a weaker disturbance of the flow near the rotor. For the surging rotor, at two rotor diameters downstream, energy from the surrounding flow is re-entrained into the wake, resulting in the disappearance of the initial differences leading to a nearly perfect superposition of the velocity profiles. However, significant differences start to appear at $x/D = 4$ for the surging cases. The velocity deficit is less pronounced for the rotor with deformable blades. At $x/D = 4$, a 6.10 % difference is observed between the minimum velocity values between the Sur-Rig and the Sur-Fle cases. Moreover, a slight reduction in the wake width is observed. This reduced wake width further indicates that blade flexibility weakens the wake deficit induced by the turbine.

Vortices emitted by the turbine for the surging rotor are shown in Fig 11. The vorticity field is plotted at $\phi_s = \pi$. Emitted vortices with vorticity magnitude $|\omega| > 0.9$ are highlighted by a white contour in the figure. Tip vortices show a delayed merging in the near wake region, compared to the rigid case. Two vortices are merging at $x/D = 0.5$ for the rigid case while the two same vortices remain distinct for flexible blades. In the $x/D > 2$ region, vorticity structures tend to move away slightly from the turbine especially around $x/R = 3.75$ for the rigid blades. Limited differences in the vorticity field can be attributed to the small differences observed in the mean aerodynamic forces. Overall, blade elasticity, within the analysed stiffness characteristics, has a limited influence on the wake development in the analysed case. The imposed surge amplitude is large compared to the blade deformations and thus, the wake development is mainly driven

by the prescribed motions.

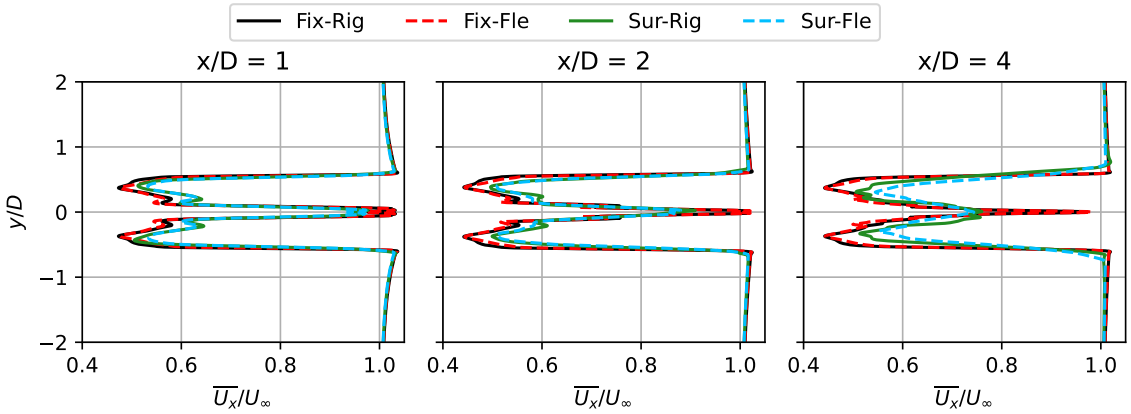

Figure 10. Time-averaged velocity profile at three positions behind the rotor

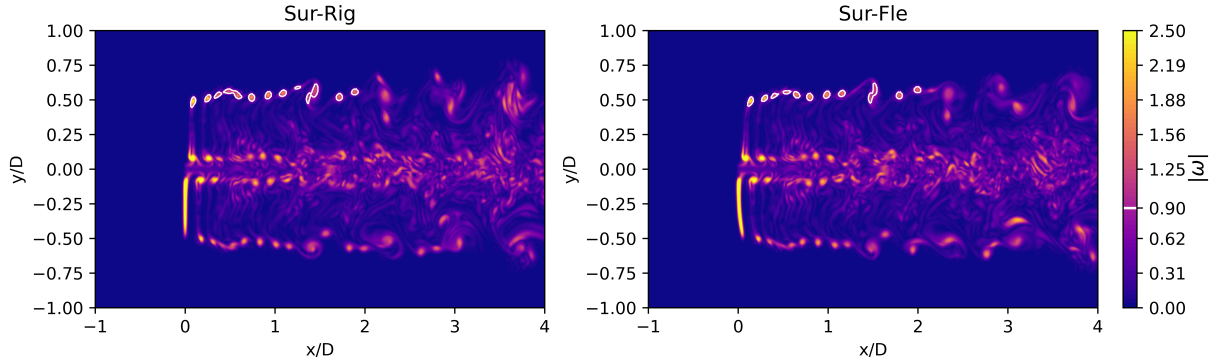

Figure 11. Vorticity field from rigid and flexible blades at maximum surge position

4. Conclusion

This study presents a structural solver based on the Timoshenko beam coupled with an ALM. The method has been verified through two cases: a fixed and a surging rotor. The ALM allows to accurately model forces on the NREL 5MW rotor and blade deflections are similar to reference values reported in the literature. For the dynamic case, consistent bending has been found with differences most probably coming from the damping model used in the structural solver and the precone angle not captured by our model.

Aeroelastic effects under imposed surge motion revealed that flexible blades change aerodynamic forces due to deformation. Differences occur near the blade tip where the deformation is maximal. In the tangential direction, the mean force is increased in comparison to the fixed rotor. Angle of attacks are modified through the surge motion. At specific instants during the oscillation, up to about half of the blade operates beyond the stall angle, increasing load unsteadiness. These dynamics also slightly influence wake development and vortex merging. In the far-wake region, larger vorticity structures develop in the rigid-blade configuration. Under the prescribed conditions, wake development is more influenced by the surge motion than by blade bending.

Future work should explore a wider range of surge amplitudes and frequencies to better characterise platform motion and FSI effects on floating offshore wind turbines.

References

[1] Bilgili M, Alphan H and Ilhan A 2023 Potential visibility, growth, and technological innovation in offshore wind turbines installed in Europe *Environmental Science and Pollution Research* **30** 27208–27226
[2] Kong C, Bang J and Sugiyama Y 2005 Structural investigation of composite wind turbine blade considering various load cases and fatigue life *Energy* **30** 2101–2114
[3] Zilic de Arcos F, Vogel C R and Willden R H 2022 A parametric study on the hydrodynamics of tidal turbine blade deformation *Journal of Fluids and Structures* **113** 103626
[4] Jonkman J M, Buhl M L *et al.* 2005 *FAST user's guide* vol 365
[5] Dose B, Rahimi H, Herráez I, Stoevesandt B and Peinke J 2018 Fluid-structure coupled computations of the NREL 5 MW wind turbine by means of CFD *Renewable energy* **129** 591–605
[6] Liu Y, Xiao Q, Incecik A and Peyrard C 2019 Aeroelastic analysis of a floating offshore wind turbine in platform-induced surge motion using a fully coupled CFD-MBD method *Wind Energy* **22** 1–20
[7] Yang L, Liao K, Ma Q, Khayyer A and Sun H 2024 Coupled aero-servo-elastic method for floating offshore wind turbine wake analysis *Ocean Engineering* **307** 118108
[8] Johlas H M, Martínez-Tossas L A, Schmidt D P, Lackner M A and Churchfield M J 2019 Large eddy simulations of floating offshore wind turbine wakes with coupled platform motion *Journal of Physics: Conference Series* vol 1256 p 012018
[9] Jonkman J and Musial W Offshore code comparison collaboration (OC3) for IEA task 23 offshore wind technology and deployment
[10] Wen B, Tian X, Dong X, Peng Z and Zhang W 2017 Influences of surge motion on the power and thrust characteristics of an offshore floating wind turbine *Energy* **141** 2054–2068
[11] Chen Z, Wang X, Guo Y and Kang S 2021 Numerical analysis of unsteady aerodynamic performance of floating offshore wind turbine under platform surge and pitch motions *Renewable Energy* **163** 1849–1870
[12] Mei Y, Jing F, Lu Q and Guo B 2024 Study on the hydrodynamic and wake characteristics of variable speed control of horizontal axis tidal turbine under surge motion *Energy* **298** 131380
[13] Jonkman J, Butterfield S, Musial W and Scott G 2009 Definition of a 5-MW reference wind turbine for offshore system development Tech. rep. National Renewable Energy Lab.(NREL), Golden, CO (United States)
[14] Hong S, McMorland J, Zhang H, Collu M and Halse K H 2024 Floating offshore wind farm installation, challenges and opportunities: A comprehensive survey *Ocean Engineering* **304** 117793
[15] Sørensen J N and Shen W Z 2002 Numerical modeling of wind turbine wakes *J. Fluids Eng.* **124** 393–399
[16] Timoshenko S 1921 On the correction for shear of the differential equation for transverse vibrations of prismatic bars *London Edinburgh Philos. Mag. J. Sci.* **41** 744–746
[17] Arabgolarcheh A, Micallef D and Benini E 2023 The impact of platform motion phase differences on the power and load performance of tandem floating offshore wind turbines *Energy* **284** 129271
[18] Xie B, Wang Y, Cai Y, Ouyang Z L, Zhu C, Tan G, Sun H and Chen Y 2025 Computational analysis of tandem floating wind turbines under coupled pitch surge motion comparing NREL 5 MW And IEA 22 MW *Scientific Reports* **15** 41381
[19] Smagorinsky J 1963 General circulation experiments with the primitive equations: I. the basic experiment *Monthly weather review* **91** 99–164
[20] Joshi J B, Nandakumar K, Patwardhan A W, Nayak A K, Pareek V, Gumulya M, Wu C, Minocha N, Pal E, Kumar M *et al.* 2019 Computational fluid dynamics *Advances of computational fluid dynamics in nuclear reactor design and safety assessment* (Elsevier) pp 21–238
[21] Churchfield M J, Schreck S J, Martinez L A, Meneveau C and Spalart P R 2017 An advanced actuator line method for wind energy applications and beyond *35th wind energy symposium* p 1998
[22] Ribeiro A F, Leweke T, Abraham A, Sørensen J N and Mikkelsen R F 2025 Blade-resolved and actuator line simulations of rotor wakes *Computers & Fluids* **287** 106477
[23] Jost E, Klein L, Leipprand H, Lutz T and Krämer E 2018 Extracting the angle of attack on rotor blades from CFD simulations *Wind Energy* **21** 807–822
[24] Zormpa M, Zilic de Arcos F, Chen X, Vogel C R and Willden R H 2025 The effect of flow sampling on the robustness of the actuator line method *Wind Energy* **28** e2965
[25] Shen W Z, Mikkelsen R, Sørensen J N and Bak C 2005 Tip loss corrections for wind turbine computations *Wind Energy* **8** 457–475
[26] Subbaraj K and Dokainish M 1989 A survey of direct time-integration methods in computational structural dynamics—II. Implicit methods *Computers & structures* **32** 1387–1401